# Terahertz conductivity of $Sr_{1-x}Ca_xRuO_3$

Diana Geiger,[1,2] Uwe S. Pracht,[1] Martin Dressel,[1] Jernej Mravlje,[3] Melanie Schneider,[4] Philipp Gegenwart,[4,*] and Marc Scheffler[1,†]

[1] *1. Physikalisches Institut, Universität Stuttgart, D-70569 Stuttgart, Germany*

[2] *Institut für Festkörperphysik, Technische Universität Wien, A-1040 Vienna, Austria*

[3] *Jozef Stefan Institute, SI-1000, Ljubljana, Slovenia*

[4] *I. Physikalisches Institut, Georg-August-Universität, D-37073 Göttingen, Germany*

(Received 24 November 2015; revised manuscript received 1 April 2016; published 22 April 2016)

We investigate the optical conductivity of $Sr_{1-x}Ca_xRuO_3$ across the ferromagnetic to paramagnetic transition that occurs at $x = 0.8$. The thin films were grown by metalorganic aerosol deposition with $0 \leqslant x \leqslant 1$ onto $NdGaO_3$ substrates. We performed terahertz frequency domain spectroscopy in a frequency range from 3 to 40 $cm^{-1}$ (100 GHz to 1.4 THz) and at temperatures ranging from 5 to 300 K, measuring transmittivity and phase shift through the films. From this we obtained the real and imaginary parts of the optical conductivity. The end-members, ferromagnetic $SrRuO_3$ and paramagnetic $CaRuO_3$, show a strongly frequency dependent metallic response at temperatures below 20 K. Due to the high quality of these samples we can access pronounced intrinsic electronic contributions to the optical scattering rate, which at 1.4 THz exceeds the residual scattering rate by more than a factor of three. Deviations from a Drude response start at about 0.7 THz for both end-members in a remarkably similar way. For the intermediate members a higher residual scattering originating in the compositional disorder leads to a featureless optical response instead. The relevance of low-lying interband transitions is addressed by a calculation of the optical conductivity within density functional theory in the local-density approximation.

DOI: 10.1103/PhysRevB.93.165131

## I. INTRODUCTION

The optical response of a material provides access to its electronic behavior in a broad window of energy scales [1]. High-frequency ultraviolet and visible light spectroscopies probe interband transitions, which give rise to an onset in the frequency-dependent optical absorption, whereas infrared and terahertz (THz) spectroscopies at lower energies provide access to more subtle aspects of the collective low-frequency response of an electron gas. One of the most interesting aspects of the collective behavior is quantum phase transitions (QPTs) [2,3]. Due to the absence of a characteristic scale near the QPT, one expects the optical response of such a material to be characterized by power laws. Power-law conductivity was found in several quantum-critical materials, such as MnSi [1,4], and in cuprates close to optimal doping [1]. It was also observed in perovskite ruthenates [1,5–8], the subject of the present paper.

The perovskite-structured ruthenate system $Sr_{1-x}Ca_xRuO_3$ is a candidate material for a ferromagnetic QPT [9–11]. Its undoped parent compound $SrRuO_3$ is an itinerant ferromagnet with ordering temperature $T_C = 160$ K and is of great interest for both fundamental physics and applications [12], whereas the other parent compound, $CaRuO_3$, is a paramagnetic metal. $CaRuO_3$ has been argued to be close to the magnetic critical point as revealed by $T^{3/2}$ temperature dependence of dc resistivity [13] below 30 K and the logarithmic term in the temperature-dependent specific heat [14]. Very recently, the observation of Shubnikov–de Haas oscillations and $T^2$ resistivity below 1.5 K revealed that a fragile Fermi liquid (FL) is recovered at low temperatures [15]. In $SrRuO_3$ the FL is more robust, with $T^2$ resistivity up to about 10 K [13,16].

THz and infrared optical studies on both compounds [5–8] revealed an unusual optical response with the optical conductivity $\hat{\sigma}(\omega) = \sigma_1(\omega) + i\sigma_2(\omega)$ distinct from that of the Drude behavior that is given by

$$\sigma_1(\omega) = \sigma_{dc}\frac{1}{1+\omega^2\tau_D^2}, \tag{1}$$

$$\sigma_2(\omega) = \sigma_{dc}\frac{\omega\tau_D}{1+\omega^2\tau_D^2}, \tag{2}$$

with $\tau_D = 1/\Gamma_D$ being the Drude scattering time and $\sigma_{dc} = 1/\rho_{dc}$ being the zero-frequency conductivity [17]. A recent optical study on clean $CaRuO_3$ samples revealed Drude behavior [15] consistent with FL concepts, but only up to a frequency of 0.6 THz. Starting from 0.6 THz, an abrupt increase of the optical scattering rate was found. A possible origin of this behavior is the coupling to a critical low-energy fluctuation.

A different point of view was offered in a very recent dynamical mean-field theory study of $CaRuO_3$ [18], which pointed out the importance of low-lying interband transitions. Namely, the orthorhombic distortion of the cubic perovskite lattice leads to a series of minigaps (with the gap size of the order of THz), which significantly affect the optical response. A related tetragonal ruthenate $Sr_2RuO_4$ that occurs in a nondistorted structure does not show low-frequency deviations and exhibits a standard FL optical response [19] instead. One needs to add, however, that $Sr_2RuO_4$ was also argued to be farther away from the quantum critical point [14].

*Present address: Experimentalphysik VI, Center for Electronic Correlations and Magnetism, Institute for Physics, Augsburg University, D-86135 Augsburg, Germany.

†marc.scheffler@pi1.physik.uni-stuttgart.de

 

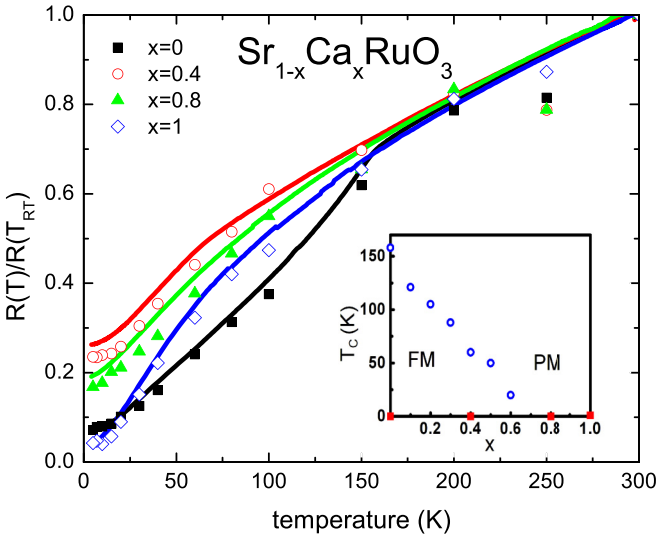


FIG. 1. Resistivity values, obtained from low-frequency optical data (symbols) and four-point dc measurements (lines). Optical relative resistivity data were calculated from low-frequency (between 4 and 5 $cm^{-1}$) THz data by normalizing to the 300 K value; dc data were normalized to the 280 K value. Inset: Phase diagram of $Sr_{1-x}Ca_xRuO_3$. Circles represent Curie temperatures of differently doped thin-film samples [20]; squares indicate the doping levels that were investigated in this optical study.

In the present work we address the evolution of the optical response of $Sr_{1-x}Ca_xRuO_3$ as a function of composition, across the magnetic phase transition. We have grown thin films, and for the compositions $x = 0$, $x = 0.4$, $x = 0.8$, and $x = 1$ (denoted by solid symbols on the phase diagram in the inset of Fig. 1) the THz response was measured. The end-members of the series are sufficiently clean to exhibit optical conductivity that corresponds to a strongly frequency-dependent scattering rate. We investigate the optical response also theoretically within density functional theory in the local-density approximation (LDA). The calculated optical scattering rate for both $CaRuO_3$ and $SrRuO_3$ shows strong frequency dependence even though frequency-independent scattering is put into the calculation; this suggests the relevance of low-lying interband transitions.

The paper is structured as follows: in Sec. II we present the details of the sample growth and the experimental setup. In Sec. III we show the measured optical conductivities and the associated optical scattering rate. In Sec. IV we present the optical conductivity as calculated within the LDA approximation and discuss the relevance of the interband transitions with respect to the experimental results. In Sec. V we summarize and conclude, and in the Appendix we analyze the scaling properties of the measured conductivities.

## II. SAMPLES AND EXPERIMENTAL SETUP

The epitaxial $Sr_{1-x}Ca_xRuO_3$ thin films were grown in Göttingen by metalorganic aerosol deposition (MAD) [21,22]. We investigated four different compositions, $SrRuO_3$, $Sr_{0.6}Ca_{0.4}RuO_3$, $Sr_{0.2}Ca_{0.8}RuO_3$, and $CaRuO_3$, all deposited on $NdGaO_3(110)$ substrates. The thin films grow epitaxially on the substrate with the same [110] orientation. $NdGaO_3$ is the substrate of choice: its lattice constant matches the thin films well, and its dielectric properties are convenient for transmittivity measurements. More precisely, for $SrRuO_3$ the substrate leads to 1.7% of compressive strain [23–25], and for $CaRuO_3$ it leads to about −0.4% of tensile strain [12,17,26]. Our measurements of the lattice constant perpendicular to the substrate are consistent with the results referenced above (not shown). Another popular substrate, $SrTiO_3$, has a very large frequency- and temperature-dependent dielectric function, which makes optical measurements difficult [27,28]. Some relevant sample properties are listed in Table I. All four samples are of high quality and clearly metallic, as evident from the resistivity curves and residual resistivity ratios (RRRs) between 300 and 0 K (extrapolated value) in Fig. 1 and Table I. While $SrRuO_3$ and $CaRuO_3$ have high RRRs of 15 and 31, respectively, the higher disorder in the $x = 0.4$ and $x = 0.8$ samples enhances the scattering and reduces the RRR to 4 and 5.

TABLE I. Properties of the studied thin-film samples. Depending on calcium content $x$, the film thickness, the Curie temperature $T_C$ determined from dc resistivity measurements (derivative), the residual resistivity ratio (RRR) from $R(300K)/R(0\,K)$ with a low-temperature extrapolation for the 0 K value, the dc resistivity value at 280 K, and the low-frequency THz resistivity value at 300 K (both used in the normalized curves in Fig. 2) are shown.

| $x$ | Thickness (nm) | $T_C$ (K) | RRR | $\rho_{dc}$ ($\mu\Omega$ cm) | $\rho_{THz}$ ($\mu\Omega$ cm) |
|---|---|---|---|---|---|
| 0 | 70 | 150 | 15 | 194 | 185 |
| 0.4 | 80 | 60 | 3.8 | 259 | 290 |
| 0.8 | 77 | | 5.4 | 215 | 230 |
| 1 | 40 | | 31 | 230 | 237 |

The transmittivity and phase response of all samples was investigated in Stuttgart in a THz frequency domain spectrometer with a Mach-Zehnder interferometer [29,30]. Figure 2 shows raw data of $CaRuO_3$ at 300 and 5 K; for comparison, the transmittivity raw data of an empty $NdGaO_3$ substrate are also plotted. A frequency range from around 3 to 40 $cm^{-1}$ was covered by measurements with five different backward wave oscillator sources [31]. The prominent Fabry-Pérot-type oscillations in the transmitted signal are typical of the raw data of metallic thin films on dielectric substrates and caused by the substrate, as indicated schematically in the inset of Fig. 2. The contribution of the film is a modulation of these substrate resonances: the difference between the data of bare $NdGaO_3$ and $CaRuO_3$ on $NdGaO_3$ in Fig. 2(a) is caused by the film. While the pure $NdGaO_3$ spectra are almost temperature independent, there is a strong temperature dependence in the thin-film samples. Already in the raw data we see a considerably lower transmittivity at 5 K than at 300 K due to increased conductivity in the metallic film. The optical conductivity is evaluated directly from the raw data: since both transmittivity and phase are measured, no Kramers-Kronig analysis is required. Each Fabry-Pérot maximum is analyzed to obtain the complex conductivity $\sigma_1$ and $\sigma_2$ at its peak frequency [16,30]. From these values, a frequency-dependent scattering rate $\Gamma(\omega)$ can be calculated using the extended

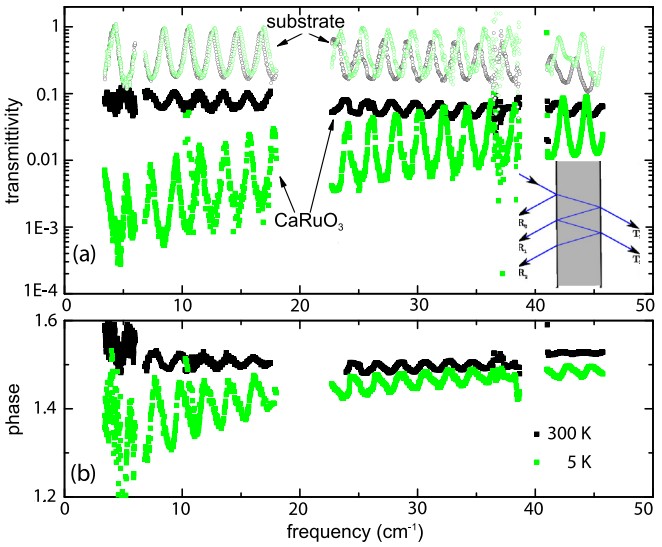


FIG. 2. (a) Transmittivity and (b) phase data of $CaRuO_3$ on $NdGaO_3$ and bare $NdGaO_3$ substrate at 300 and 5 K. Open circles correspond to substrate data; solid squares correspond to thin-film samples. The inset in (a) shows that multiple reflections in a dielectric substrate lead to Fabry-Pérot oscillations in the raw data.

Drude formalism:

$$\frac{\Gamma(\omega)}{\epsilon_0\omega_P^2} = \rho_1(\omega) = \frac{\sigma_1(\omega)}{\sigma_1(\omega)^2 + \sigma_2(\omega)^2}, \tag{3}$$

with $\omega_P = \sqrt{ne^2/\epsilon_0 m}$ being the plasma frequency, $e$ and $m$ being the (free-)electron charge and mass, $n$ being the charge carrier density, and $\epsilon_0$ being the vacuum permittivity [16,32]. The real part $\rho_1(\omega)$ of the frequency-dependent resistivity is directly proportional to the scattering rate $\Gamma(\omega)$ and can be determined from experimental data without knowledge of $\omega_P$. Therefore, we will use $\rho_1$ as a measure for the scattering rate when we discuss its frequency and temperature dependence.

## III. RESULTS

Figure 3 shows the frequency-dependent real and imaginary parts of the conductivity of all samples. The absolute values of $\sigma_1$ are characteristic of metals and of the order of $10^4\ \Omega^{-1}\ \mathrm{cm}^{-1}$. At temperatures above 100 K, all samples show nearly frequency independent real and low imaginary parts: the scattering rate exceeds our measured frequency range. A maximum in $\sigma_1(\omega)$ has been observed in the midinfrared at these temperatures [1,7]. In our data there is no visible onset of this maximum; $\sigma_1(\omega)$ drops monotonically [33]. In Fig. 1 we compare the THz response at our low-frequency limit [in particular the real part $\rho_1$ of the frequency-dependent resistivity $\hat{\rho}(\omega) = \rho_1(\omega) + i\rho_2(\omega) = 1/\hat{\sigma}(\omega)$] with results from dc measurements. There is very good agreement between these two data sets. This suggests that at least in this temperature range there are no additional features in the optical conductivity at lower frequencies. Considering that dc resistivity current paths and THz beam spots do not necessarily probe the same sample areas, Fig. 1 also documents the homogeneity of the films.

### A. $SrRuO_3$

The $\sigma_1$ and $\sigma_2$ spectra of $SrRuO_3$ for exemplary temperatures are shown in Figs. 3(a) and 3(e), respectively. The $\sigma_1$ spectrum, rather flat at high temperatures, changes upon cooling: below 40 K, $\sigma_1(\omega)$ develops a drop towards higher frequencies that moves to lower frequencies, down to around 12 $\mathrm{cm}^{-1}$, with decreasing temperature. In terms of the Drude formula (1) this drop indicates the scattering rate $\Gamma/2\pi$.

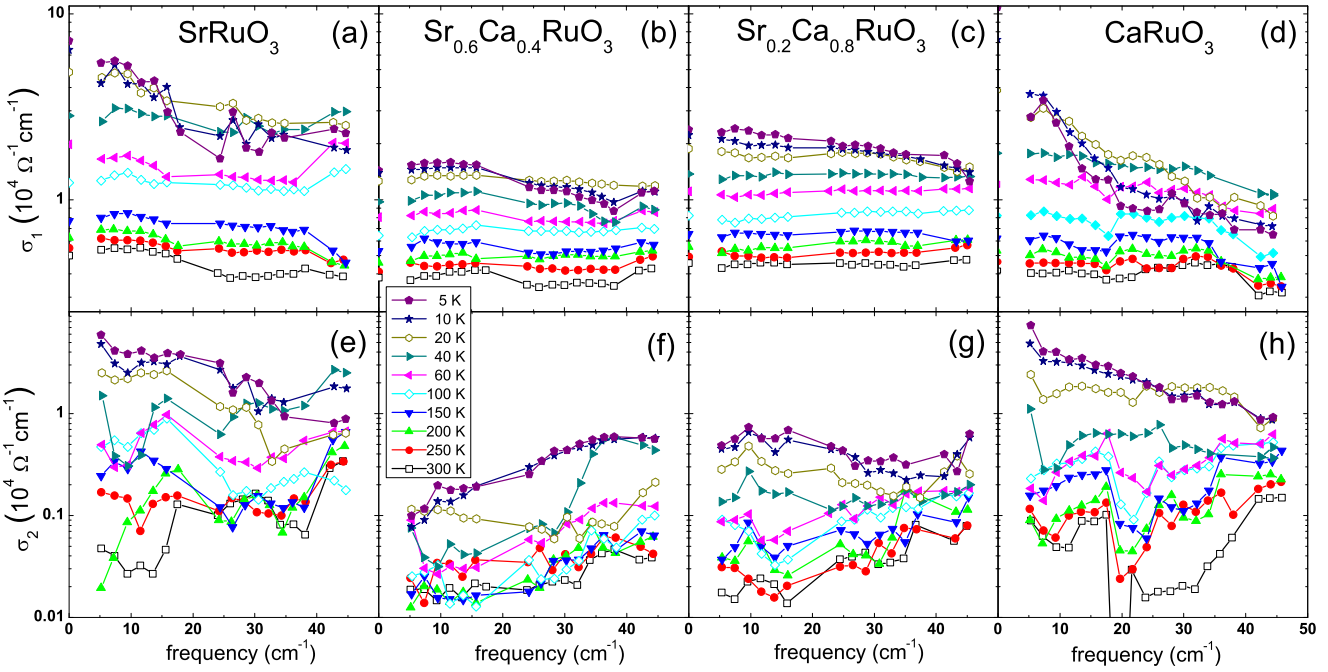


FIG. 3. Real and imaginary parts of the optical conductivity of the four studied $Sr_{1-x}Ca_xRuO_3$ compositions at various temperatures between 300 and 5 K [33,35].

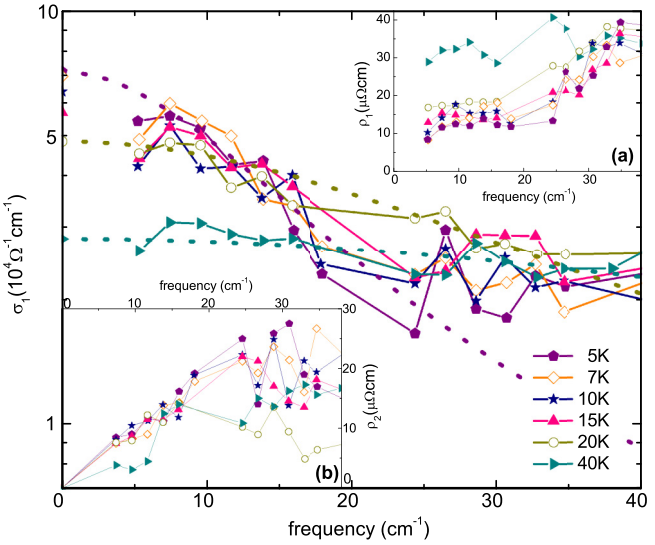


FIG. 4. $\sigma_1(\omega)$ of $SrRuO_3$ for low temperatures. The dotted lines at 5, 20, and 40 K are Drude fits following Eq. (1) with $\sigma_{dc}$ values fixed from dc measurements. All points were taken into account for the 20 and 40 K fits; the 5 K fit includes only frequencies below 30 $cm^{-1}$ due to the non-Drude-like plateau at higher frequencies. Insets (a) and (b) show $\rho_1$ and $\rho_2$ for corresponding temperatures, respectively.

To be consistent with a Drude interpretation, $\sigma_2(\omega)$ should show a maximum at the corresponding frequency, passing through our spectral range as a function of temperature [34] and leaving monotonous frequency-dependent behavior in the limiting cases, namely, increasing with frequency for high temperatures and decreasing for low temperatures, as found in our data. To address the low-temperature properties of $SrRuO_3$ in more detail, Fig. 4 shows $\sigma_1(\omega)$ for all measured temperatures below 40 K. In addition, we show Drude fits following Eq. (1) for a few temperatures. Within the measurement accuracy, the Drude fits describe the conductivity data well above 20 K. However, at lower temperatures, the conductivity of $SrRuO_3$ deviates from the Drude fit because at high frequencies $\sigma_1(\omega)$ is not reduced further upon cooling but remains constant.

This plateau for frequencies above 20 $cm^{-1}$ is present in all spectra in Fig. 4 and becomes more evident with decreasing temperature. Since the plateau cannot be described as part of a single Drude term, the fit at 5 K only includes the points below 30 $cm^{-1}$. For further analysis we use the extended Drude formalism, Eq. (3). The obtained $\rho_1$, which is proportional to the scattering rate, is shown in Fig. 5(a) for the same temperatures as in Fig. 3. Above 40 K the scattering rate is basically constant as a function of frequency, corresponding to a simple Drude behavior. Below 20 K, Fig. 5(a) indicates a pronounced frequency dependence of the scattering rate, an increase towards higher frequencies.

Deviations from Drude behavior were noticed earlier by Dodge *et al.* [6]. Our $\sigma_1(\omega)$ of $SrRuO_3$ qualitatively follows this: flat for high temperatures with a broad low-frequency peak emerging at lowest temperatures. The high quality of our samples, achieved with MAD [22], leads to 2–3 times higher absolute values of $\sigma_1$ at low temperatures compared to earlier experiments [6], which enables us to characterize those deviations in better detail.

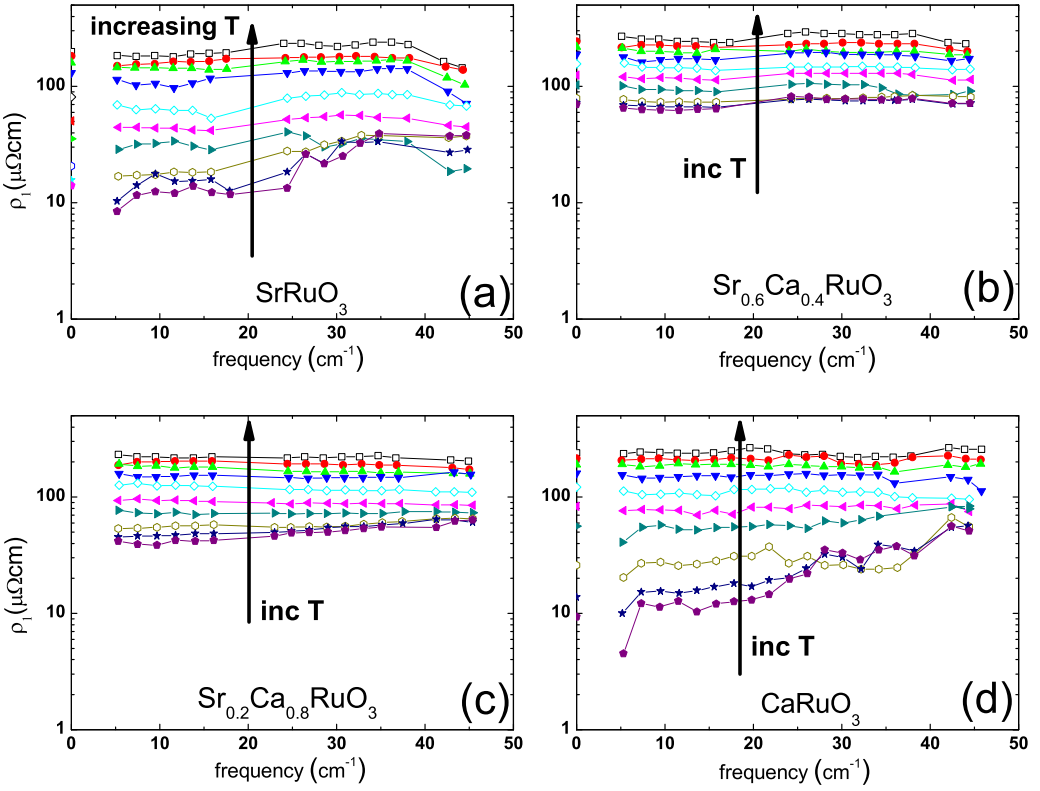


FIG. 5. Frequency-dependent $\rho_1$, proportional to the scattering rate $\Gamma$, at 300, 250, 200, 150, 100, 60, 40, 20, 10, and 5 K. Colors and symbols are as in Fig. 3.

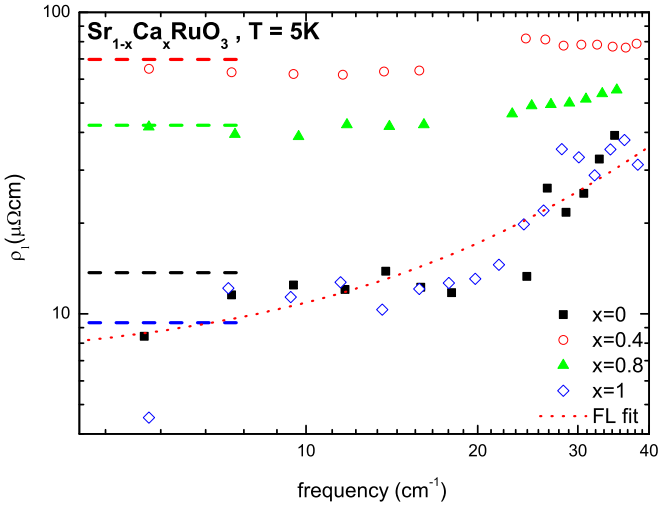


FIG. 6. Real part $\rho_1$ of complex resistivity, proportional to the scattering rate $\Gamma$, of $Sr_{1-x}Ca_xRuO_3$ at 5 K. The dashed guides indicate the value of the dc value, $1/\sigma_{dc}$. The dotted line indicates the best FL-like fit to the entire data range.

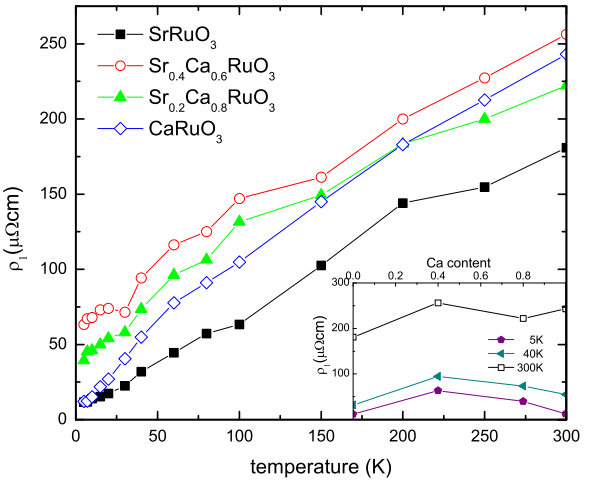


FIG. 7. $\rho_1$, proportional to the scattering rate $\Gamma$, from extended Drude analysis at frequency 7 $cm^{-1}$ for the four different compositions $Sr_{1-x}Ca_xRuO_3$ as a function of temperature (main plot) and as a function of Ca content $x$ (inset).

For this purpose we turn to Fig. 6, where $\rho_1$ at 5 K is plotted. It is mostly frequency independent below 20 $cm^{-1}$, in the range below the plateau in $\sigma_1(\omega)$. Above 20 $cm^{-1}$ it increases strongly with frequency, approximately by a factor of three between 20 and 35 $cm^{-1}$. While the high-frequency points do not contradict a quadratic frequency dependence, a FL fit $\rho_0 + A\omega^2$ over the entire frequency range does not reproduce the measured data well (dotted line in Fig. 6).

In order to investigate this point in more detail, we turn to inset (b) in Fig. 4, which shows the imaginary part $\rho_2(\omega)$ of the frequency-dependent resistivity. $\rho_2(\omega)$ is proportional to the frequency-dependent effective mass, which in turn is related to the memory function, and in a FL $\rho_2(\omega)$ is theoretically expected to show linear frequency dependence [19,36]. Our data are consistent with this expectation only up to 20 $cm^{-1}$. At higher frequencies a saturation is seen, which cannot be interpreted in FL terms.

The observed THz conductivity above 20 $cm^{-1}$ is hence inconsistent with what one would expect of a FL, and another explanation for the non-Drude behavior in this frequency range has to be found. A possible explanation is that interband transitions are activated at these frequencies [18]. We discuss this possibility in the theoretical part of the paper (Sec. IV).

### B. $Sr_{0.6}Ca_{0.4}RuO_3$ and $Sr_{0.2}Ca_{0.8}RuO_3$

The conductivity spectra of the doped samples are shown in Figs. 3(b), 3(c), 3(f), and 3(g). For both compositions, $\sigma_1(\omega)$ is almost constant, and $\sigma_2$ is much smaller than $\sigma_1$; this suggests a conventional metallic conductivity where the scattering rate is much higher than the studied spectral range. A weak frequency dependence only emerges at the lowest temperatures. Upon cooling, both $\sigma_1(\omega)$ and $\sigma_2(\omega)$ increase, which is consistent with a decrease in scattering rate. From the comparison of all samples in Fig. 3 we find that the conductivity of the doped samples is substantially lower than that of the undoped ones. This we attribute to compositional disorder, which significantly increases the residual scattering. As expected, this effect is more pronounced for $Sr_{0.6}Ca_{0.4}RuO_3$, where the disorder due to the composition will be particularly strong. This scenario is consistent with the comparatively small increase of the conductivity upon cooling and, correspondingly, with the small residual resistivity ratio. In contrast to the undoped samples the frequency dependence of $\sigma_1$ is weaker: $\sigma_1(\omega)$ at low optical frequencies is similar to the dc value. The extended Drude analysis yields a mostly frequency independent $\rho_1$ and therefore scattering rate (Fig. 5), substantially higher at low temperatures than in the pure compounds (Fig. 6). Therefore, the strong disorder scattering in the doped samples dominates their transport properties at low temperatures, which makes it impossible to deduce signatures of electronic correlations from the THz data at this stage. This is unfortunate, as $Sr_{0.2}Ca_{0.8}RuO_3$ is located close to the QPT from ferromagnetism to paramagnetism, and here the influence of quantum-critical fluctuations to the electronic scattering would be of particular interest.

That the high scattering rate at low temperatures in these two samples indeed stems from the disorder is illustrated by a comparison with the pure compounds in Fig. 7. The main plot shows $\rho_1$ as a function of temperature, determined from the extended Drude analysis at 7 $cm^{-1}$, for all samples of this study. The scattering rates of $Sr_{0.6}Ca_{0.4}RuO_3$ and $Sr_{0.2}Ca_{0.8}RuO_3$ basically are shifted to higher values when compared to $SrRuO_3$, and this temperature-independent offset is stronger for $Sr_{0.6}Ca_{0.4}RuO_3$. The inset of Fig. 7 shows $\rho_1 \propto \Gamma$ as a function of Ca content $x$ for three exemplary temperatures. At the lower temperatures, the dome-shaped dependence with minimal scattering for the pure compounds at the two outer ends and a maximum around the center is evident.

### C. $CaRuO_3$

$CaRuO_3$ exhibits a behavior similar to $SrRuO_3$: at high temperatures, $\sigma_1(\omega)$ is almost constant throughout our spectral range, and $\sigma_2(\omega)$ is very small [see Figs. 3(d) and 3(h)]. This

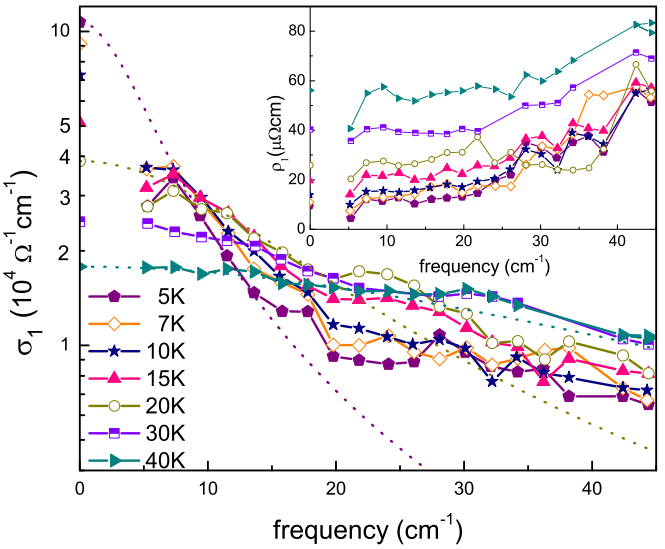


FIG. 8. $\sigma_1$ spectra of $CaRuO_3$ for low temperatures with tentative Drude fits. Due to the high-frequency plateau, the fits do not work at lowest temperatures. Inset: Scattering rates for corresponding temperatures.

is consistent with a frequency-independent scattering rate, as shown in Fig. 5(d). Upon cooling, $\sigma_1$ and $\sigma_2$ continuously increase; down to approximately 40 K the frequency dependence of $\sigma_1(\omega)$ as well as $\Gamma(\omega)$ is weak. This changes at lower temperatures (see Fig. 8): at frequencies below 10 $cm^{-1}$, $\sigma_1$ strongly increases, while at higher frequencies it is rather constant or even slightly decreasing. Hence, at the lowest temperatures, e.g., 5 K, a rapid roll-off is seen in $\sigma_1(\omega)$ as a function of frequency: $\sigma_1$ at the lowest optical frequencies is already considerably lower than $\sigma_{dc}$. The roll-off is followed by a plateau, which is distinct from what is expected from the Drude response. The frequency-dependent scattering rate is proportional to the real part of the resistivity $\rho_1$, which was extracted from the extended Drude analysis. $\rho_1$ is shown in Fig. 5(d), and the 5 K one is compared to the other compositions in Fig. 6.

The optical data for $CaRuO_3$ were discussed earlier by Schneider *et al.* [17], and they were found to be inconsistent with Drude or FL behavior [36] above $\sim$20 $cm^{-1}$. The deviations from Drude behavior are displayed also in Fig. 8. The high quality of the $CaRuO_3$ sample is evident from the low scattering rate at lowest temperatures, as clearly discernible from the comparison with the other samples in Fig. 7. With increasing temperature, this low-frequency scattering rate increases more strongly than for $SrRuO_3$ (and the intermediate samples) due to stronger electronic correlations in the absence of ferromagnetism [37].

In previous optical studies on $CaRuO_3$, Lee *et al.* mainly focused on data above 40 $cm^{-1}$ in a large temperature range without measuring many low temperatures [7]. This study has a substantial overlap in temperature and frequency range with that of Kamal *et al.* [8]. Our conductivity spectra match these two previous works well and are consistent if quantitative shifts due to our enhanced film quality are taken into account. In our study, the most pronounced frequency and temperature dependence of the conductivity is located at the lowest energies: temperatures below 20 K and frequencies below 10 $cm^{-1}$, beyond the limits of the previous works. Scaling plots were proposed and were controversially discussed in Lee *et al.* [7] and Kamal *et al.* [8]. To compare with these earlier works, we replotted our data in the suggested form (see the Appendix). Our data on $SrRuO_3$ do not scale well. For $CaRuO_3$, the scaling seems to be obeyed, but as was discussed in Ref. [8], the accessible frequency and temperature ranges are too narrow, and the noise level is too high to draw any firm conclusions.

## IV. LOW-FREQUENCY OPTICAL CONDUCTIVITY WITHIN LDA

Very recently, it was argued that low-lying optical interband transitions, which are activated by orthorhombic distortions, might affect the optical response at unexpectedly low frequencies. In particular, a dynamical mean-field theory (DMFT) study [18] argued that the low-frequency deviation from Drude optics in $CaRuO_3$ occurs already at the level of band theory. As a test for the effects of the band structure in the simplest possible setting, we calculated the optical conductivity of $SrRuO_3$ and $CaRuO_3$ (in their bulk structure) using LDA as implemented in the WIEN2K package [38,39]. In this approach, the current matrix elements are evaluated from the band structure, and the optical conductivity is evaluated for a frequency-independent scattering rate as described by a self-energy $\Sigma = -i(1/\tau_D)/2$. A similar approach was used in iron-based superconductors [40,41] in which interband contributions were also found to be important.

The frequency-dependent real part of the optical conductivity, normalized to the zero-frequency value, is displayed in Fig. 9. One sees that the calculated optical conductivities for orthorhombic structures deviate from the Drude behavior $\sigma_1(\omega)/\sigma_{dc} = 1/(1+\omega^2\tau_D^2)$ at very low frequencies of the

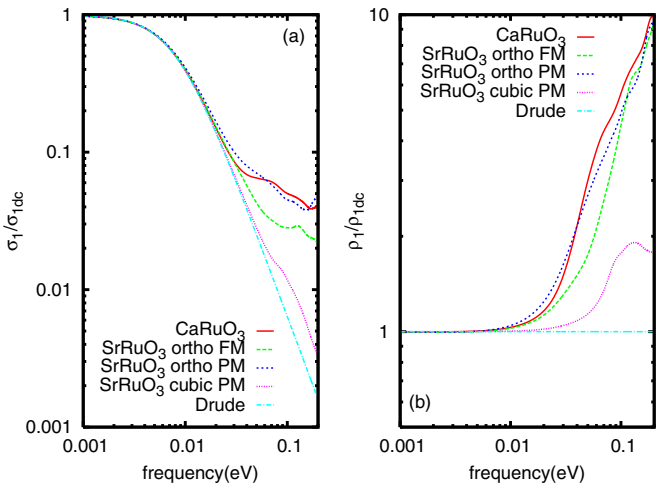


FIG. 9. (a) Optical conductivity in the LDA approximation with static impurity scattering $1/\tau_D = 0.008$ eV for $CaRuO_3$ and for $SrRuO_3$ compared to the Drude optical conductivity. For $SrRuO_3$, besides ferromagnetic calculation in an orthorhombic structure, the paramagnetic result in the orthorhombic and cubic structure are also shown. (b) The corresponding optical scattering rates, normalized to the dc value.

order of 20 meV. These deviations originate in low-lying interband transitions across minigaps that are opened up by orthorhombic distortions. Nonmagnetic $SrRuO_3$ shows a behavior very similar to that of $CaRuO_3$ but with obvious deviations from Drude behavior at even lower frequencies, which is due to the fact that the orthorhombic distortion is smaller there. The shift of the bands due to the exchange splitting in ferromagnetic $SrRuO_3$ (with moment $1.6\mu_B$) diminishes these deviations. The calculated optical conductivity in the cubic structure deviates from the Drude behavior starting at a higher frequency and in a much less pronounced way.

For easier comparison with the experimental data, we extracted also $\rho_1(\omega) = \mathrm{Re}[1/\hat{\sigma}(\omega)]$, which is proportional to the optical scattering rate as defined by the extended Drude formalism. This presents a very clear influence of the band-structure effect. Although the actual scattering rate put into the calculation is frequency independent, the inferred optical scattering rate (that attempts to describe the response of a multiband system in terms of the response of a single-band one) exhibits a strong frequency dependence.

In these calculations, $SrRuO_3$ and $CaRuO_3$ show a deviation from the Drude dynamics at similar frequencies of about 20 meV. To compare this value to the frequency in the experiment, one needs to additionally divide the value by the corresponding renormalizations. In $CaRuO_3$, the measured specific heat is about 7 times above the value found in the band theory [42]. Therefore, the expected frequency for the deviation from Drude dynamics is 20 meV/7 $\approx$ 3 meV ($\approx$0.7 THz $\approx$ 24 $cm^{-1}$) and is consistent with the experiment.

In $SrRuO_3$ the renormalization is smaller, about 4 judging from the specific heat [43]. Furthermore, mostly the minority carriers (with the plasma frequency $\omega_{p\downarrow} \sim 2.6$ eV) and not the majority carriers (which correspond to small Fermi surfaces of the almost completely filled bands and the plasma frequency $\omega_{p\uparrow} \sim 1.3$ eV) contribute to the conductivity, and within LDA+DMFT it was found [18] that the renormalization for these minority carriers is smaller, only about 2.

From these considerations, the deviation from Drude behavior through band structure effects would only be expected at a frequency scale above our experimental range. However, one needs to keep in mind that the growth of $SrRuO_3$ on the $NdGaO_3$ substrate modifies the structure substantially [23,24], which may decrease the corresponding scale. This should be tested in future theoretical calculations or experimentally by growth on different substrates.

## V. CONCLUSIONS AND OUTLOOK

The optical conductivity of the four samples, $SrRuO_3$, $Sr_{0.6}Ca_{0.4}RuO_3$, $Sr_{0.2}Ca_{0.8}RuO_3$, and $CaRuO_3$, of the material system $Sr_{1-x}Ca_xRuO_3$ with a QPT at $x \approx 0.8$ were investigated with THz spectroscopy. The transmittivity and phase data revealed metallic behavior for all samples. The doped samples have a comparably high scattering rate due to compositional disorder, and their THz properties can be described within a simple Drude picture. The $SrRuO_3$ and $CaRuO_3$ samples, in contrast, at low temperatures have low scattering rates consistent with the high RRRs that could be achieved by MAD growth. At low temperatures, $SrRuO_3$ and $CaRuO_3$ can be described by a Drude response with a constant scattering rate only up to approximately 20 $cm^{-1}$. By calculating the optical response within the band theory we have shown that the deviations from Drude behavior may be caused by low-lying interband transitions. Especially for $CaRuO_3$, the calculated response is very similar to the measured one, whereas for $SrRuO_3$ the calculated scattering rate deviates at a frequency that is too high to account for our measurements. A possible origin of this discrepancy is a deviation of the thin-film structure from the bulk one for which the calculations were made, an issue that needs to be explored in future work.

On the experimental side, future studies should, on the one hand, attempt to reach lower temperatures [30,44,45] and frequencies [46,47], in particular to check if the crossover to a scattering rate quadratic in frequency that would indicate the elusive FL optical response [32,48–58] can be found. Furthermore, optical measurements on our MAD-grown samples at higher frequencies, in the infrared range, should be performed to allow direct comparison with previous studies of samples with somewhat lower RRR at infrared frequencies and to further investigate the nature of the non-Drude plateau. At these larger frequencies not only the band effects but also the genuine contribution from correlations [18] will contribute.

Further improvement in sample growth can be envisaged, too. While the scattering rate for doped samples with random arrangement of Sr and Ca atoms will remain too high to reveal interesting behavior in our frequency range, further improvements of the residual scattering of $CaRuO_3$ thin films have recently been achieved by growth on $NdGaO_3$ substrates with vicinal cut [17]. THz studies of such samples might be more difficult due to birefringence in the substrate [59,60], but finally, such studies might reveal even more clearly the unconventional scattering rate of $CaRuO_3$ at THz frequencies.

## ACKNOWLEDGMENTS

D.G. acknowledges the support of the Austrian Science Fund (FWF) doctoral program W1243 Solids4Fun. U.S.P acknowledges support from the Studienstiftung des deutschen Volkes. J.M. acknowledges the support of the Slovenian Research Agency (ARRS) under Program P1-0044. We acknowledge financial support from the Deutsche Forschungsgemeinschaft (DFG).

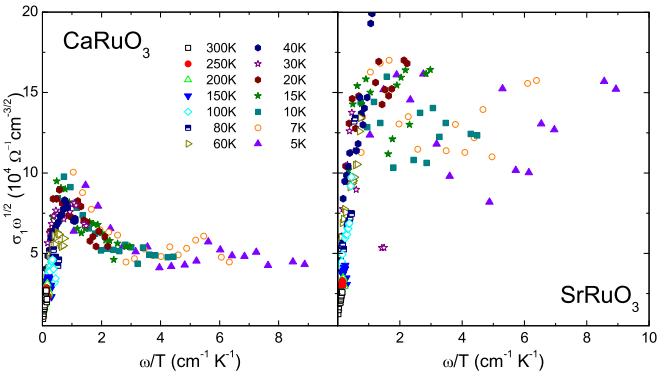


FIG. 10. $\omega/T$ scaling plots for $SrRuO_3$ and $CaRuO_3$ following Refs. [7,8].

## APPENDIX: SCALING ANALYSIS

Previous optical studies found that $\sigma_1(\omega,T)$ data for $SrRuO_3$ and $CaRuO_3$ can be combined into a scaling plot following

$$\sigma_1(\omega,T) = \omega^{-1/2} Z(\omega/T), \tag{A1}$$

with scaling function $Z(\omega/T)$ [7,8]. Such scaling of an experimentally accessible response can be a strong indication for quantum-critical behavior [61,62], but the initial suggestion [7] that the apparent scaling of $\sigma_1(\omega,T)$ in $SrRuO_3$ and $CaRuO_3$ should be interpreted as quantum critical was later rebutted [8]. To present our data in the context of the scaling analysis of those previous works, we plot $\sigma_1(\omega,T)\omega^{1/2}$ vs $\omega/T$ in Fig. 10, which should lead to data collapse if Eq. (A1) were appropriate to describe the data. While our high-temperature spectra collapse into a small region of the scaling plot for both samples, below 40 K the samples differ strongly: in the case of $CaRuO_3$, within the experimental error, all temperatures collapse to one scaling curve, which slightly broadens for lower temperatures. For $SrRuO_3$ the spectra fail to collapse below 40 K. Although $CaRuO_3$ and $SrRuO_3$ show similar features in their optical conductivities and scattering rates, they are different with respect to the low-energy scaling behavior. Our low-frequency and low-temperature spectra of $SrRuO_3$ cannot be scaled by expression (A1), while it works well for $CaRuO_3$.


[1] D. N. Basov, R. D. Averitt, D. van der Marel, M. Dressel, and K. Haule, Rev. Mod. Phys. **83**, 471 (2011).

[2] T. Vojta, Ann. Phys. (Leipzig) **9**, 403 (2000).

[3] H. V. Löhneysen, A. Rosch, M. Vojta, and P. Wölfle, Rev. Mod. Phys. **79**, 1015 (2007).

[4] F. P. Mena, D. van der Marel, A. Damascelli, M. Fäth, A. A. Menovsky, and J. A. Mydosh, Phys. Rev. B **67**, 241101(R) (2003).

[5] P. Kostic, Y. Okada, N. C. Collins, Z. Schlesinger, J. W. Reiner, L. Klein, A. Kapitulnik, T. H. Geballe, and M. R. Beasley, Phys. Rev. Lett. **81**, 2498 (1998).

[6] J. S. Dodge, C. P. Weber, J. Corson, J. Orenstein, Z. Schlesinger, J. W. Reiner, and M. R. Beasley, Phys. Rev. Lett. **85**, 4932 (2000).

[7] Y. S. Lee, J. Yu, J. S. Lee, T. W. Noh, T. H. Gimm, H. Y. Choi, and C. B. Eom, Phys. Rev. B **66**, 041104 (2002).

[8] S. Kamal, D. M. Kim, C. B. Eom, and J. S. Dodge, Phys. Rev. B **74**, 165115 (2006).

[9] G. Cao, S. McCall, M. Shepard, J. E. Crow, and R. P. Guertin, Phys. Rev. B **56**, 321 (1997).

[10] P. Khalifah, I. Ohkubo, H. M. Christen, and D. G. Mandrus, Phys. Rev. B **70**, 134426 (2004).

[11] D. Fuchs, C. L. Huang, J. Schmalian, M. Wissinger, S. Schuppler, K. Grube, and H. V. Löhneysen, Eur. Phys. J. Spec. Top. **224**, 1105 (2015).

[12] G. Koster, L. Klein, W. Siemons, G. Rijnders, J. S. Dodge, C. B. Eom, D. H. A. Blank, and M. R. Beasley, Rev. Mod. Phys. **84**, 253 (2012).

[13] L. Capogna, A. P. Mackenzie, R. S. Perry, S. A. Grigera, L. M. Galvin, P. Raychaudhuri, A. J. Schofield, C. S. Alexander, G. Cao, S. R. Julian, and Y. Maeno, Phys. Rev. Lett. **88**, 076602 (2002).

[14] G. Cao, O. Korneta, S. Chikara, L. E. DeLong, and P. Schlottmann, Solid State Commun. **148**, 305 (2008).

[15] M. Schneider, D. Geiger, S. Esser, U. S. Pracht, C. Stingl, Y. Tokiwa, V. Moshnyaga, I. Sheikin, J. Mravlje, M. Scheffler, and P. Gegenwart, Phys. Rev. Lett. **112**, 206403 (2014).

[16] A. P. Mackenzie, J. W. Reiner, A. W. Tyler, L. M. Galvin, S. R. Julian, M. R. Beasley, T. H. Geballe, and A. Kapitulnik, Phys. Rev. B **58**, R13318(R) (1998).

[17] M. Dressel and G. Grüner, *Electrodynamics of Solids* (Cambridge University Press, Cambridge, 2002).

[18] H. T. Dang, J. Mravlje, A. Georges, and A. J. Millis, Phys. Rev. Lett. **115**, 107003 (2015).

[19] D. Stricker, J. Mravlje, C. Berthod, R. Fittipaldi, A. Vecchione, A. Georges, and D. van der Marel, Phys. Rev. Lett. **113**, 087404 (2014).

[20] M. Schneider, V. Moshnyaga, and P. Gegenwart, Phys. Status Solidi B **247**, 577 (2010).

[21] V. Moshnyaga, I. Khoroshun, A. Sidorenko, P. Petrenko, A. Weidinger, M. Zeitler, B. Rauschenbach, R. Tidecks, and K. Samwer, Appl. Phys. Lett. **74**, 2842 (1999).

[22] M. Schneider, V. Moshnyaga, and P. Gegenwart, J. Phys. Conf. Ser. **200**, 012178 (2010).

[23] R. Aso, D. Kan, Y. Shimakawa, and H. Kurata, Cryst. Growth Des. **14**, 2128 (2014).

[24] A. T. Zayak, X. Huang, J. B. Neaton, and K. M. Rabe, Phys. Rev. B **77**, 214410 (2008).

[25] W. Lu, W. Song, P. Yang, J. Ding, G. Moog Chow, and J. Chen, Sci. Rep. **5**, 10245 (2015).

[26] A. Vailionis, W. Siemons, and G. Koster, Appl. Phys. Lett. **93**, 051909 (2008).

[27] D. Geiger, M. Scheffler, M. Dressel, M. Schneider, and P. Gegenwart, J. Phys. Conf. Ser. **391**, 012091 (2012).

[28] M. M. Felger, M. Dressel, and M. Scheffler, Rev. Sci. Instrum. **84**, 114703 (2013).

[29] B. P. Gorshunov, A. A. Volkov, A. S. Prokhorov, and I. E. Spektor, Phys. Solid State **50**, 2001 (2008).

[30] U. S. Pracht, E. Heintze, C. Clauss, D. Hafner, R. Bek, S. Gelhorn, D. Werner, M. Scheffler, M. Dressel, D. Sherman, B. Gorshunov, K. S. Il'in, D. Henrich, and M. Siegel, IEEE Trans. Terahertz Sci. Technol. **3**, 269 (2013).

[31] In the experimental part, $cm^{-1}$ (wave numbers) will be used as a unit of frequency, which is common for spectroscopy experiments in this frequency range. It refers to the number of wavelengths per unit length (or "cycles per unit length") and is related to the wavelength $\lambda$ and the frequency in hertz $f_{Hz}$ by $f_{cm^{-1}} = 1/\lambda = f_{Hz}/c$ ($c$ represents the speed of light). The energy conversion to other common units is 1 $cm^{-1} \hat{=}$ 29.98 GHz $\hat{=}$ 0.124 meV.

[32] M. Scheffler, K. Schlegel, C. Clauss, D. Hafner, C. Fella, M. Dressel, M. Jourdan, J. Sichelschmidt, C. Krellner, C. Geibel, and F. Steglich, Phys. Status Solidi B **250**, 439 (2013).

[33] Our measured data start with dc measurements ($f = \omega/2\pi = 0$), followed by frequencies from around 5 to 40 $cm^{-1}$. We find that at the lowest frequencies it becomes increasingly difficult to obtain precise values for the conductivity because of stray radiation: a fraction of the comparatively broad THz beam can reach the detector without interfering with the sample and therefore can cause a higher experimentally determined transmittivity. This becomes most evident at high conductivity values because the absolute signal strength is already very low. In our measurements with highest $\sigma_1$ (found in the undoped samples at low temperatures) the lowest-frequency point is lower than expected. We attribute this feature to stray radiation and do not interpret it in terms of a physical property of the sample.

[34] M. Dressel and M. Scheffler, Ann. Phys. (Leipzig) **15**, 535 (2006).

[35] At the highest frequencies, correspondingly, at the shortest wavelength, the THz phase measurement is more difficult, thus leading to less reliable data in $\sigma_2$ and $\rho_1$, which in our case might be particularly the case for the measurements on the rather thick $SrRuO_3$ sample, with its low overall THz transmitted signal, above 40 $cm^{-1}$.

[36] C. Berthod, J. Mravlje, X. Deng, R. Žitko, D. van der Marel, and A. Georges, Phys. Rev. B **87**, 115109 (2013).

[37] H. T. Dang, J. Mravlje, A. Georges, and A. J. Millis, Phys. Rev. B **91**, 195149 (2015).

[38] P. Blaha, K. Schwarz, G. Madsen, D. Kvasnicka, and J. Luitz, *WIEN2K, An Augmented Plane Wave + Local Orbitals Program for Calculating Crystal Properties* (Technische Universitat Wien, Vienna, 2001).

[39] C. Ambrosch-Draxl and J. Sofo, Comput. Phys. Commun. **175**, 1 (2006).

[40] L. Benfatto, E. Cappelluti, L. Ortenzi, and L. Boeri, Phys. Rev. B **83**, 224514 (2011).

[41] M. J. Calderón, L. de' Medici, B. Valenzuela, and E. Bascones, Phys. Rev. B **90**, 115128 (2014).

[42] M. Shepard, S. McCall, G. Cao, and J. E. Crow, J. Appl. Phys. **81**, 4978 (1997).

[43] P. B. Allen, H. Berger, O. Chauvet, L. Forro, T. Jarlborg, A. Junod, B. Revaz, and G. Santi, Phys. Rev. B **53**, 4393 (1996).

[44] N. Bachar, U. S. Pracht, E. Farber, M. Dressel, G. Deutscher, and M. Scheffler, J. Low. Temp. Phys. **179**, 83 (2015).

[45] D. N. Basov, S. V. Dordevic, E. J. Singley, W. J. Padilla, K. S. Burch, J. E. Elenewski, L. H. Greene, J. Morris, and R. Schickling, Rev. Sci. Instrum. **74**, 4703 (2003).

[46] M. Scheffler and M. Dressel, Rev. Sci. Instrum. **76**, 074702 (2005).

[47] K. Steinberg, M. Scheffler, and M. Dressel, Rev. Sci. Instrum. **83**, 024704 (2012).

[48] M. Dressel, J. Phys. Condens. Matter **23**, 293201 (2011).

[49] K. Yoshimura, T. Imai, T. Kiyama, K. R. Thurber, A. W. Hunt, and K. Kosuge, Phys. Rev. Lett. **83**, 4397 (1999).

[50] R. N. Gurzhi, Sov. Phys. JETP **35**, 673 (1959).

[51] P. E. Sulewski, A. J. Sievers, M. B. Maple, M. S. Torikachvili, J. L. Smith, and Z. Fisk, Phys. Rev. B **38**, 5338 (1988).

[52] U. Nagel, T. Uleksin, T. Rõõm, R. P. S. M. Lobo, P. Lejay, C. C. Homes, J. S. Hall, A. W. Kinross, S. K. Purdy, T. Munsie, T. J. Williams, G. M. Luke, and T. Timusk, PNAS **109**, 19161 (2012).

[53] T. Katsufuji and Y. Tokura, Phys. Rev. B **60**, 7673 (1999).

[54] J. Yang, J. Hwang, T. Timusk, A. S. Sefat, and J. E. Greedan, Phys. Rev. B **73**, 195125 (2006).

[55] D. N. Basov, E. J. Singley, and S. V. Dordevic, Phys. Rev. B **65**, 054516 (2002).

[56] S. I. Mirzaei, D. Stricker, J. N. Hancock, C. Berthod, A. Georges, E. van Heumen, M. K. Chan, X. Zhao, Y. Li, M. Greven, N. Bari, and D. van der Marel, Proc. Natl. Acad. Sci. USA **110**, 5774 (2013).

[57] A. V. Chubukov and D. L. Maslov, Phys. Rev. B **86**, 155136 (2012).

[58] D. L. Maslov and A. V. Chubukov, Phys. Rev. B **86**, 155137 (2012).

[59] M. Scheffler, J. P. Ostertag, and M. Dressel, Opt. Lett. **34**, 3520 (2009).

[60] J. P. Ostertag, M. Scheffler, M. Dressel, and M. Jourdan, Phys. Rev. B **84**, 035132 (2011).

[61] A. Schröder, G. Aeppli, R. Coldea, M. Adams, O. Stockert, H. V. Löhneysen, E. Bucher, R. Ramazashvili, and P. Coleman, Nature (London) **407**, 351 (2000).

[62] O. Stockert, H. V. Löhneysen, W. Schmidt, M. Enderle, and M. Loewenhaupt, J. Low Temp. Phys. **161**, 55 (2010).